Nano Energy 115 (2023) 108684

Contents lists available at ScienceDirect

Nano Energy

journal homepage: www.elsevier.com/locate/nanoen

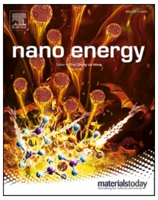

Stabilized bismuth nanoplasmonics for selective CO_2 reduction to methanol at a heterointerface

Haijiao Lu[a,1], Nasir Uddin[a,1], Zhehao Sun[a,1], Zibin Chen[b,*], Zackaria Mahfoud[c], Yilan Wu[d], Ary Anggara Wibowo[e], Zhicheng Su[f,g], Xinmao Yin[h,i], Chi Sin Tang[j], Xiaozhou Liao[k], Simon P. Ringer[k], Xiu Song Zhao[d], Hieu T. Nguyen[e], Andrew T.S. Wee[i], Michel Bosman[c,l,**], Zongyou Yin[a,*]

[a] Research School of Chemistry, Australian National University, ACT 2601, Australia
[b] Department of Industrial and Systems Engineering, The Hong Kong Polytechnic University, Hung Hom, Hong Kong, China
[c] Institute of Materials Research and Engineering, A*STAR (Agency for Science, Technology and Research), 2 Fusionopolis Way, 138634, Singapore
[d] School of Chemical Engineering, The University of Queensland, St Lucia, QLD, 4072 Australia
[e] School of Engineering, The Australian National University, Canberra, ACT 2601, Australia
[f] School of Electronic Science and Engineering, Southeast University, Nanjing, Jiangsu 210096, China
[g] Department of Electronic Materials Engineering, Research School of Physics, The Australian National University, Canberra, ACT 2601, Australia
[h] Shanghai Key Laboratory of High Temperature Superconductors, Physics Department, Shanghai University, Shanghai, 200444, China
[i] Department of Physics, Faculty of Science, National University of Singapore, 117542, Singapore
[j] The Singapore Synchrotron Light Source (SSLS), National University of Singapore, 117603, Singapore
[k] School of Aerospace, Mechanical and Mechatronic Engineering, The University of Sydney, Sydney, NSW 2006, Australia
[l] Department of Materials Science and Engineering, National University of Singapore, 9 Engineering Drive 1, 117575, Singapore

ARTICLE INFO

Keywords:
Photocatalysis
CO_2 reduction
Methanol
LSPR
Heterointerface

ABSTRACT

Photocatalytic CO_2 transformation into value-added chemicals has enormous industrial importance, but is challenging to operate with multifaceted performances in activity, selectivity, stability and regenerability. We successfully achieved this goal by integrating plasmonic bismuth nanoparticles and non-plasmonic redox heterojunctions. This maximizes the product selectivity by directing the reaction paths via the electric field of localized surface plasmon resonances (LSPRs). We attach non-noble plasmonic Bi particles with a shell of BiOCl to self-assembled TiO_2 nanosheets, creating a transformative hybrid plasmonic nanostructure for CO_2-to-methanol conversion. It exhibits high photoactivity (235.26 μmol g^{-1} h^{-1}), outstanding selectivity (~90 % sole carbon/methanol product, ~10 % H_2) and is free of backward reactions, thanks to the synergistic effects of the hybrid nanostructure: complementary light absorption, strong local fields, and an adaptive redox heterojunction. Macro-to-micro experiments and simulations reveal that the BiOCl shell is responsible for stabilizing Bi to generate robust LSPRs, to induce 7–9 times local field enhancement, enabling efficient and selective CO_2-to-methanol conversion at the TiO_2-BiOCl heterointerfaces. This work demonstrates a durable and easily-regenerable photocatalyst with the capability to tune the CO_2 reduction pathway by plasmon fields. Moreover, it provides a unique paradigm to harvest hydrogen carriers (liquid methanol and hydrogen gas) from the greenhouse gas CO_2.

1. Introduction

Currently, about 8 % of total anthropogenic CO_2 emissions comes from aviation and shipping, which will further increase with the growth in global trade and tourism [1,2]. Carbon-neutral transportation is becoming feasible with electric motors powered by rechargeable batteries, but highly challenging, if not impossible, for long-haul flights [3]. An alternative solution is to break the carbon-loop by directly storing solar energy into transportable liquid fuels via CO_2 reduction. Methanol is a critical chemical of significant importance. It is a clean fuel and an

---

[*] Corresponding authors.

[**] Corresponding author at: Department of Materials Science and Engineering, National University of Singapore, 9 Engineering Drive 1, 117575, Singapore.

E-mail addresses: zi-bin.chen@polyu.edu.hk (Z. Chen), msemb@nus.edu.sg (M. Bosman), zongyou.yin@anu.edu.au (Z. Yin).

[1] These authors contributed equally to this work

https://doi.org/10.1016/j.nanoen.2023.108684
Received 6 November 2022; Received in revised form 27 June 2023; Accepted 8 July 2023

essential building block for ~30 % of known chemicals. More attractively, methanol is an alternative promising carrier of hydrogen (12.5 wt % high gravimetric hydrogen content at ambient conditions) [4,5]. Thus, solar-driven CO_2 photoreduction to methanol (CO_2PRM) has been intensively studied, as methanol is a stable liquid with low viscosity (~0.54 mPa·s) easier for storage and transportation than hydrogen gas [4,5]. In the CO_2PRM processes, the challenges lie in the catalytic efficiency, selectivity and stability. As summarized in Table S1, a wide variety of noble metal-free photocatalysts have been developed in the past decade for sacrificial agent-free CO_2PRM. The efficiency of CO_2PRM has been well recorded, but ~66 % of these works did not report the selectivity due to the challenges caused by the diverse products from the CO_2 reduction reaction. In these studies, the highest methanol generation rate was 510 μmol g^{-1} h^{-1} with unclear selectivity, while the catalysts were only photoactive under UV light (< 5 % of the solar spectrum energy) with short performance stability (40 mins) [6]. On the other hand, the reported catalysts with the best selectivity and stability (~83 % and 12 h) suffer from a mediocre efficiency in methanol production (~114 μmol g^{-1} h^{-1}) [7]. Undoubtedly, it will be a major milestone in CO_2 conversion to achieve an excellent balance between efficiency, selectivity and stability.

The performance of a photocatalyst is mainly determined by three steps: light absorption, electron-hole separation and surface reaction. Forming heterojunction of two functional components (e.g., semiconductor/semiconductor, semiconductor/metal) is widely being applied in photocatalyst design, as summarized in our recent review [8]. However, when it comes to CO_2 reduction, taking CO_2PRM as an example, it requires six electrons to complete the multiple hydrogenation steps and the reaction path dominates the selectivity and hence the carbon product species. To improve the efficiency, stability and selectivity of photocatalysts for CO_2 reduction, the integration of plasmonic nanoparticles (NPs) and a non-plasmonic heterojunction has emerged as an effective strategy [9–11].

Some studies have examined the synergistic effects of plasmonic NPs and a non-plasmonic heterojunction for CO_2 photoreduction where product selectivity is considerably varied [12–15] and some issues are still unsolved. First, noble metal particles are uncontrollably randomly grown onto the heterojunction [16] which will downgrade the tunability of their plasmonic function. Second, heteroepitaxy [12] and selective photodeposition [13,14] synthesis strategies enable a component-located growth of plasmonic metals onto heterojunctions, and likewise yolk-shell structures result in direct noble metal growth on the shell [15]. However, the electric field (E-field) from localized surface plasmon resonances (LSPRs) will be exponentially decreased when it reaches the heterojunction interface. This reduces the power of the local E-field to promote charge-carriers involved in redox reactions at the interfaces of the designed junction. Third, research has mainly focused on noble metals (Au, Ag, Pt) as plasmon-active NPs, as they are inert and resistant to air and water; unfortunately, their high cost hinders the upscaling for practical applications. Fourth, plasmon-active non-noble metals such as Cu, Al, Ni, and Bi have attracted much interest due to their low cost and high availability and they have been studied in some applications including CO_2 photoreduction [17]. However, their susceptibility to corrosion even under ambient conditions, requires optimization to achieve higher stability for practical use. Last but not the least, the effect of non-noble metal plasmons on the selectivity in CO_2 photoreduction is still largely unknown.

This work combines theory and experiments to rigorously demonstrate a catalytic system that combines the advantages of LSPRs and heterojunctions with high activity, high selectivity, and excellent regenerability. The system consists of core-shell bismuth-based NPs attached to self-assembled TiO_2 nanosheets (NSs). A reduction-crystallization synthetic route was developed to construct the core-shell (Bi-BiOCl) NPs on TiO_2 NSs. Our results present the properties of these hybrid nanostructures and how the LSPR in combination with the BiOCl shell boosts the CO_2 reduction. Predictive simulations were employed to understand the underlying mechanism on how the LSPR-induced E-field is formed at the plasmonic/dielectric interface, penetrates the dielectric layer, and then tailors the CO_2 reduction paths at the redox heterojunction. The system is then optimized to achieve efficient, multielectron-demanding CH_3OH production from CO_2 reduction.

2. Results and discussion

2.1. Synthesis and characterization

The compositions and crystal structures of the as-prepared photocatalyst were characterized with mutiple techniques. In Fig. 1a, the powder X-ray diffraction (pXRD) patterns of the single components show the major characteristic peaks of anatase TiO_2 at $2\theta = 25.41^\circ$ (JCPDS card no. 21–1272) [18,19] and tetragonal BiOCl (JCPDS card no. 06–0249) [20–22] respectively. No diffraction peaks related to Bi_2O_3 impurities [23] are observed, implying the high purity of the as-obtained BiOCl. The intense and sharp diffraction peaks at $2\theta = 24.46$, 26.27, 32.75, 33.78, 35.08 and 36.89° indicate that the as-prepared BiOCl has high crystallinity. After coupling of TiO_2 and BiOCl, the as-prepared photocatalyst exhibits a few new intense peaks at $2\theta = 27.23$, 38.01 and 39.75°, corresponding to rhombohedral Bi NPs (JCPDS card no. 05–0519) [24,25]. However, the disappearance of all representative BiOCl peaks in the formed TiO_2-BiOCl-Bi heterojunction (henceforth called 'fresh sample'), suggests that BiOCl may have an amorphous structure or poor crystallinity after $NaBH_4$ treatment. Note that $NaBH_4$ treatment along with Ar annealing does play a key role in the reduction of superficial BiOCl into metallic Bi and the features above are maintained for all studied samples (Note S1, Fig. S1-S2). In the X-ray photoelectron spectroscopy (XPS) spectrum of the Bi 4 f edge (Fig. 1b), the peaks at 165.08 and 159.78 eV can be indexed to Bi 4 $f_{5/2}$ – 4 $f_{7/2}$ lines (energy spacing 5.3 ± 0.1 eV), implying that bismuth is in the Bi^{3+} state in BiOCl, whilst those at 162.81 and 157.51 eV in the fresh sample correspond to metallic Bi^0 [22,24,26]. The branching ratio between these major peaks is about 1.33 (Bi 4 $f_{7/2}$/ Bi 4$f_{5/2}$ ~ 0.99/0.74) which is consistent with previous reports [27]. XPS spectra of Ti 2p, Cl 2p and O1s are all in good agreement with the literature [28,29] as shown in Fig. S3.

UV-Vis/DRS (diffuse reflectance spectroscopy) (Fig. 1c) was measured to study the light absorption properties of the as-prepared catalysts. The spectra of BiOCl and TiO_2 display distinct absorption that tail into the UV and visible light regions, respectively. After forming the heterojunction, a broad absorption band emerges between 450 and 600 nm absorption, signalling the LSPR effect attributed to metallic bismuth within the as-prepared heterostructure [30,31]. Fig. 1d shows the PL emission spectra of TiO_2 and as-prepared TiO_2-BiOCl-Bi samples to evaluate the charge recombination properties. The stronger PL intensity indicates more charge recombination under light irradiation [32]. Therefore, the spectra suggest that the charge recombination of TiO_2-BiOCl-Bi-fresh is significantly suppressed compared with that of TiO_2, which can be attributed to the photoexcited charge carrier separation and transfer across the junction between TiO_2 and BiOCl. Note that both the PL peak intensities at ~455 nm (bulk features of TiO_2) [33], and ~600 nm (surface defect sites, e.g. oxygen vacancies) [34,35] show similar significant quenching, implying effective charge separation for both bulk TiO_2 and for surface defects at the TiO_2-BiOCl-Bi heterojunction.

The morphology of the synthesized materials was characterized by scanning electron microscopy (SEM), as shown in Fig. 1e and Fig. S4. Fig. S4a shows that ultrathin TiO_2 NSs 100–200 nm in diameter self-assemble to form hierarchical spheres, in good agreement with the literature [18]. BiOCl-Bi NPs (Fig. S4b) of spherical shape aggregate due to their large surface energy, and variations in molar ratios (TiO_2:Bi=20, 15, 10) yield three variants of the samples, namely TB 20-post-Ar (TiO_2: Bi=20:1, molar ratio, post Ar annealing treatment) (Fig. S4c), TB 15-post-Ar (15:1) (Fig. 1e, Fig. S4d), and TB 10-post-Ar (10:1) (Fig. S4e).

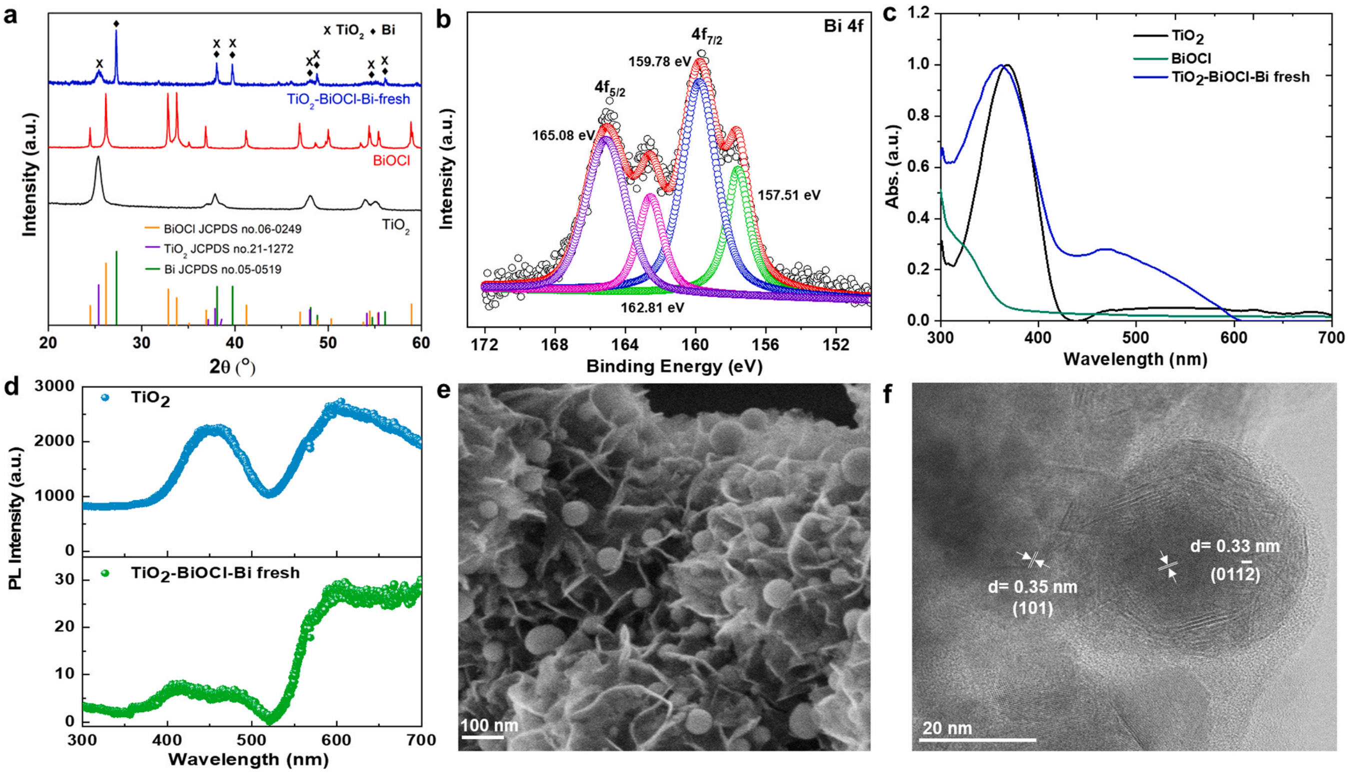

Fig. 1. Structural analysis and characterization of the studied photocatalysts. (a) pXRD patterns of TiO_2-BiOCl-Bi, BiOCl and TiO_2 NSs samples in comparison with JCPDS cards no.06–0249 (BiOCl), no.21–1272(TiO_2), and no.05–0519 (Bi). (b) High resolution XPS spectrum of Bi 4 f in a TiO_2-BiOCl-Bi fresh sample. (c) UV-Vis/DRS of TiO_2-BiOCl-Bi, BiOCl and TiO_2 NSs samples. (d) PL spectra of TiO_2-BiOCl-Bi and TiO_2 NSs samples. (e) SEM image and (f) HRTEM image of the TiO_2-BiOCl-Bi fresh sample.

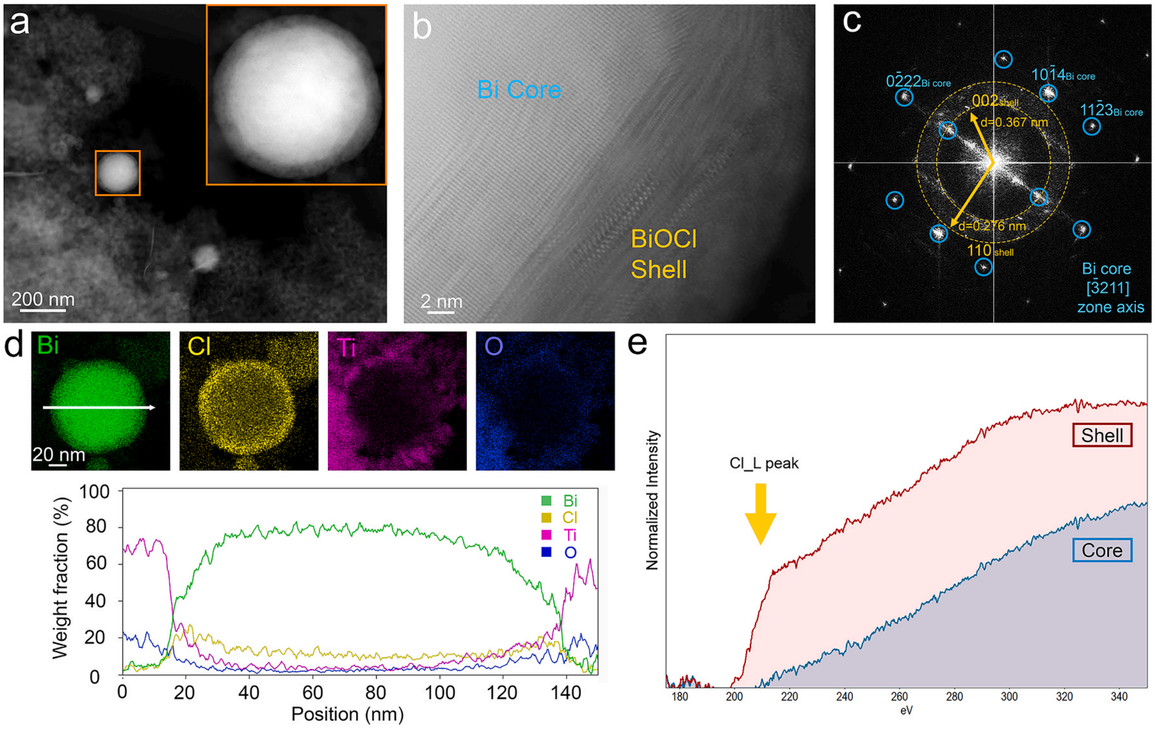

Fig. 2. STEM-EELS analysis of core-shell structure in TiO_2-BiOCl-Bi heterojunction. (a) A STEM-HAADF image of the TiO_2-BiOCl-Bi catalyst. Inset is a STEM-HAADF image of a core-shell NP. (b) An atomic-resolution STEM-HAADF image of the Bi core and BiOCl shell. (c) An FFT image of the core-shell structure. (d) elemental mapping and line scan of the selected core-shell regions and weight fractions of Bi, Cl, Ti, and O elements. (e) representative EELS spectra of the Bi core and BiOCl shell showing the presence of the Cl L edge.

With increasing Bi molar percentage, the loading ratio of Bi NPs on TiO_2 NSs formed by in-situ borohydrite reduction increases accordingly. Due to the low ratio of Bi NPs in TB 20-post-Ar, they distribute unevenly between the TiO_2 NSs. In comparison, the distribution of Bi NPs in TB 15-post-Ar with higher Bi content is more uniform than that in TB 20-post-Ar. When the molar ratio of Bi further increases, Bi NPs fill-up the gaps between TiO_2 NSs and even cover the surface of the TiO_2 hierarchical spheres in TB 10-post-Ar, which is unfavourable as it blocks the exposure of TiO_2 to the environment. If not specified in this work, the TiO_2-BiOCl-Bi in the following text refers to the TB 15-post-Ar sample (TiO_2:Bi=15:1, molar ratio, post Ar annealing treatment). High-resolution TEM (HRTEM) images show TiO_2 lattice spacings of 0.35 nm, which is attributable to the (101) planes, whilst the characteristic lattice spacings of 0.33 nm measured in the core correspond to the (0$\bar{1}$2) planes of Bi (Fig. 1f).

Scanning transmission electron microscopy (STEM)-based analysis was performed for nanoscale characterization of the morphology of NPs and the spatial distribution of elements in the heterojunction. Fig. 2a shows randomly-distributed core-shell NPs with well-defined morphologies on the TiO_2 matrix. A core-shell heterojunction with Bi core and BiOCl shell (~8 nm) is clearly observed (Fig. 2a, inset). Enlarged atomic-resolution STEM-HAADF (high-angle annular dark field) images of the NPs show the crystalline characteristics of the Bi core and disordered lattice fringes of the BiOCl shell (Fig. 2b). The disordered lattice fringes with short-range ordered structures in the BiOCl shell are in line with XPS and XRD results. To further examine the structure of the core-shell NPs, corresponding fast Fourier transforms (FFTs) were studied (Fig. 2c). The Bi core possesses an R$\bar{3}$m trigonal structure, and is projected here along the [$\bar{3}$211] zone axis. Some disordered reflections were measured from the BiOCl shell, with d-spacing values of 0.367 and 0.276 nm, from the (002) and (110) planes, which are also observed in the crystalline pure BiOCl sample, i.e. those located at $2\theta = 24.46^\circ$ and 32.75° of the red curve in Fig. 1a, respectively [36]. These reflections were not detected by XRD due to the very small signal of the 8 nm thick BiOCl shell in comparison with the much larger volumes of TiO_2 and Bi in the XRD samples. STEM, on the other hand, directly shows the local atomic structure of the BiOCl shell, allowing us to confirm the presence of the disordered lattice fringes. The elemental maps and line scan analysis confirms that the shell mainly consists of Bi, O, and Cl, while the core possesses a large amount of Bi (Fig. 2d). Electron energy-loss spectroscopy (EELS) measurements were also carried out to confirm the Cl elemental distribution across the core-shell heterojunction, as shown in Fig. 2e. A sharp and strong Cl_L peak is observed from the shell, confirming the presence of Cl in the shell structure. A weak Cl_L peak is also seen in the central part of the NP, which comes from the overlap of the projected shell along the viewing direction, and does not indicate any presence of Cl in the core.

2.2. *Performance of plasmonic TiO_2-BiOCl-Bi systems*

As discussed above, the TiO_2-BiOCl-Bi synthesized in this work, compared with TiO_2, exhibits a broader solar-spectrum absorption with enhanced photoexcited charge carrier separation and transfer across the heterojunction interface. The photoactivity of these materials was assessed for CO_2 reduction under solar illumination at ambient conditions. As displayed in Fig. 3a, TiO_2 NSs (S1) can only produce H_2 gas, while BiOCl-Bi and TB 15-pre-Ar (i.e, TiO_2-BiOCl-Bi sample before annealing treatment) does not lead to any identifiable products. After annealing, significantly higher H_2 and CH_3OH generation rates were observed for TiO_2-BiOCl-Bi samples decorated with different ratios of Bi NPs. Both the H_2 and CH_3OH generation rates first increase with decreasing TiO_2: Bi molar ratios from 20:1–15:1 (TB 15-post-Ar), and then decrease with further decreased TiO_2: Bi molar ratios beyond 10:1. Among all our studied photocatalysts, TB 15-post-Ar shows the highest generation rates of both H_2 and CH_3OH, demonstrating its superior photoactivity. Although the LSPR effect from a higher ratio of Bi NPs can contribute to the improvement of photoactivity, overloading with Bi NPs will shield TiO_2 from light and thus reduce its photogeneration of charge

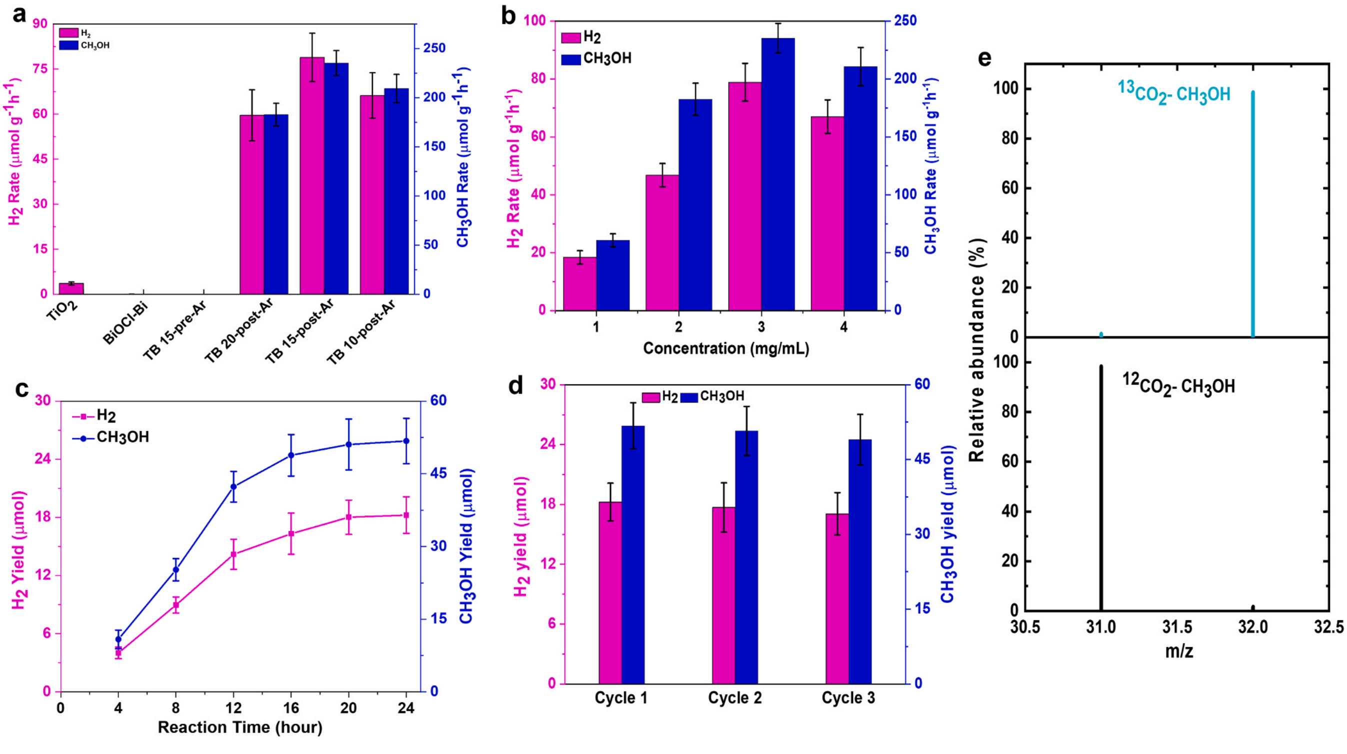

Fig. 3. Photocatalytic CO_2 reduction activity. (a) Differently-prepared catalytic materials against H_2 and CH_3OH production rates. (b) Concentration effect on H_2 and CH_3OH production rate. (c) Illuminated reaction time against H_2 and CH_3OH production. (d) Stability test for 3 consecutive cycles and (e) mass spectra for the obtained C-containing species from $^{13}CO_2$ experiment over the optimal TiO_2-BiOCl-Bi (TB 15-post-Ar) catalysts.

carriers. Therefore, considering the trade-off between the LSPR effect and the light shielding effect of Bi NPs, TiO_2-BiOCl-Bi photocatalysts should be decorated with an optimal ratio of Bi NPs to achieve the highest photoactivity. As TB 15-post-Ar is our optimal photocatalyst, this sample was studied in more depth for the rest of this work.

As revealed in Fig. 3b, the optimal concentration of TB 15-post-Ar photocatalyst turned out to be 3 mg/mL, which exhibits the highest generation rates for both H_2 (78.89 μmol g^{-1} h^{-1}) and CH_3OH (235.26 μmol g^{-1} h^{-1}). The photostability of the optimal photocatalyst was further studied by comparing the H_2 and CH_3OH yields over a long reaction period up to 24 h. As observed from Fig. 3c, the yields for both H_2 and CH_3OH increased almost linearly with time during 0–12 h, followed by a declining increment until 24 h, indicating the gradual deactivation of photoactivity. Furthermore, the photoactivity of the regenerated catalyst was evaluated by 3 cycles of 24-h photocatalytic CO_2 reduction. Both the H_2 and CH_3OH yields are well maintained after the 1st and 2nd round of regeneration, as shown in Fig. 3d. Post-reaction investigation of pXRD (Fig. S5), UV-Vis/DRS (Fig. S6), XPS (Fig. S7) and PL (Fig. S8) measurements reveal that the structural configurations and properties of the photocatalysts remain identical as that of TB 15-post-Ar, implying the durability and regenerability of the catalysts, and therefore the possibility of widespread industrial application. More importantly, the TB 15-post-Ar sample generates methanol as the only C-containing product with a selectivity of ~90 % against ~10 % hydrogen fuel, while bare TiO_2 samples just yield hydrogen as the only product (Note S2). The wavelength-dependent catalytic CO_2 reduction was also investigated with the CH_3OH and H_2 production rates summarized in Fig. S10 of Note S2. The results show that the production rates of CH_3OH

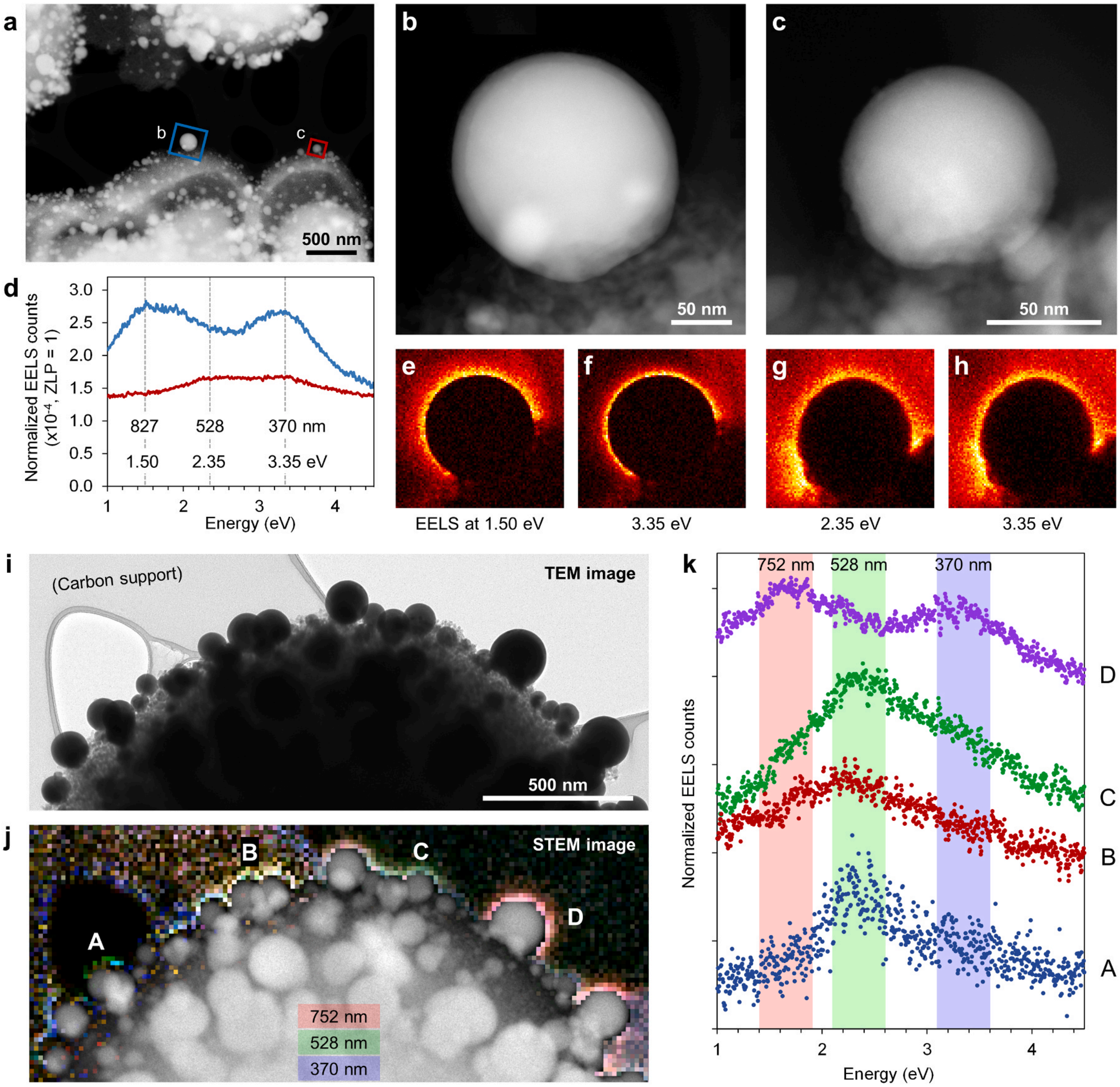

Fig. 4. Spectroscopy on individual Bi NPs, local variations in optical response and localized surface plasmon resonance modes in core-shell structures. (a) STEM-HAADF overview image of TiO_2 covered with variously-sized Bi NPs, with two typical NPs marked: (b) a large Bi NP (radius of 93 nm), and (c) a small Bi NP (radius of 46 nm). (d) Monochromated EELS spectra from the large (blue) and from the small (red) Bi NPs, normalized to compare their relative intensities. (e) EELS map of the large Bi NP at 1.50 eV and (f) at 3.35 eV, corresponding to the first and second peaks in the blue spectrum. EELS map of the small Bi NP (g) at 2.35 eV and (h) at 3.35 eV, the two main peaks in the red spectrum. The peaks at 3.35 eV correspond to optical absorption at a wavelength of 370 nm, as indicated in panel (d). (i) TEM image of a TiO_2 support (dark, area at the bottom) covered with variously-sized Bi NPs. (j) STEM-HAADF image in grayscale overlaid with three monochromated EELS maps acquired in the same area at 752 nm (red), 528 nm (green) and 370 nm (blue). The geometry of the detector only allows EELS signal to be measured from the edges of the TiO_2 support. (k) EELS spectra from locations A-D in the STEM image. The red, green and blue shades indicate the energy ranges of 1.4–1.9 eV, 2.1–2.6 eV, and 3.1–3.6 eV, corresponding with the three respective EELS maps. The TEM carbon support film on the left gives a weak EELS background signal unrelated to the plasmon losses of the bismuth NPs.

and H_2 decreased with the light wavelength prolonged from 380, 400, 500–600 nm, while the molar ratio between CH_3OH and H_2 was not significantly affected. The apparent quantum efficiency (AQE) is nearly 1.14 % at 400 nm, demonstrating the effectiveness of photon utilization for CH_3OH production from CO_2 (Note S2). Although H_2 gas is also obtained as a result of the competing hydrogen evolution reaction in the aqueous environment, it is automatically separated from methanol in the liquid phase and can be collected and used as an ultraclean fuel [7]. Afterwards, isotope-labeled experiments were conducted to confirm that methanol is produced through photoreduction of CO_2 rather than photocatalytic reaction of carbon contaminations. Results in Fig. 3e indicate that the $^{13}CO_2$ source leads to a strong signal at $m/z = 32$, which corresponds to ^{13}C methanol, while the signal from the $^{12}CO_2$ source is distinctly located at $m/z = 31$ (Fig. S11). This verifies that the detected methanol is produced from the photoreduction of CO_2 over the TiO_2--BiOCl-Bi photocatalysts. We further carried out various control experiments to exclude the possibility that methanol was produced in other ways (Note S3, Fig. S11-13).

2.3. *Monochromated STEM-EELS plasmon analysis and simulations*

We ascribe the selective methanol generation over hydrogen evolution in CO_2 reduction to the local field enhancement, at the TiO_2-BiOCl hetero-interfaces and the utilization of Bi plasmons [37,38]. The LSPR effect of the plasmonic Bi from the TiO_2-BiOCl-Bi heterostrucutre gives rise to strong optical absorption, scattering, and electromagnetic field confinement, which will affect the reaction dynamics [39]. To gain insights into the enhanced light absorption by the plasmonic Bi NPs, monochromated EELS combined with STEM-HAADF imaging was carried out to measure the local optical response of the Bi NPs [40]. Fig. 4a shows the variously-sized core-shell Bi-BiOCl NPs on TiO_2 nanosheets. In Fig. 4b-c, two core-shell NPs with a radius of ~93 and ~46 nm, respectively, were selected as examples to reveal the impact of particle size on the plasmonic properties. The EELS spectrum of the larger core-shell NP shows two absorption peaks, at 1.50 and 3.35 eV, assigned to metallic Bi and BiOCl, respectively, corresponding to light absorption at wavelengths of 827 and 370 nm (Fig. 4d, blue line). In addition, two weaker peaks, at 2.35 and again 3.35 eV (corresponding to light absorption at a wavelength of 528 and 370 nm, respectively) were observed for the smaller Bi-BiOCl NPs (Fig. 4d, red line). The results indicate that the Bi-BiOCl NPs of both sizes have LSPR effects (Fig. 4e-h), and that the particle size has significant impact on the light absorption. Further study on local variations in optical response was carried out. Fig. 4i shows that variously-sized Bi-BiOCl NPs are dispersed on TiO_2 nanosheets nonuniformly. Four example locations, A-D, are indicated in Fig. 4j and the spectra from these locations are given in Fig. 4k. All spectra have either a peak or weak shoulder with different height ratios around 3.35 eV (370 nm, near-UV) and 2.35 eV (528 nm, visible: green), while D shows an additional peak at 1.50 eV (752 nm, red/near-IR). As indicated by the legend of Fig. 4j, these three wavelengths are mapped in blue, green and red. In this overlay-image of an area with differently-sized NPs, mixed colours are seen in many locations. Although the BiOCl shell only absorbs the UV light, the variously-sized Bi core NPs can absorb light ranging from the UV, visible to the near IR region, endowing this core-shell structure with the capability of broad-wavelength-range light absorption. This EELS study provides evidence for the LSPR phenomenon of the Bi NPs and their capacity for broad, tunable light harvesting. EELS simulations of small and large Bi-BiOCl NPs presented in Fig. S15–16 confirm the strong tunability of the plasmon response by controlling the size of the particles.

Although the LSPR effect has been widely used to enhance the photocatalytic activity of semiconductors such as TiO_2, the underlying mechanism is still not fully understood [41]. Direct contact between the plasmonic metal and TiO_2 is not necessary for photocatalytic enhancement, and has been attributed to the increase in the electromagnetic field by the presence of LSPRs [42]. A close proximity between TiO_2 and a non-stable plasmonic material such as Bi can be achieved with a dielectric layer to separate them, while stabilizing the plasmonic metal; such a geometry is provided by our metal/dielectric core/shell NPs. The properties of local electromagnetic fields induced by the surface plasmon resonances in a core-shell system can be tuned by changing the radius of the metallic core or the thickness of the dielectric shell (Note S4, Fig. S14–15). As displayed by the spectra in Fig. 5a, increasing the size of the metallic core induces a redshift of the resonances and the appearance of a new peak. This redshift is a typical plasmonic effect: the increased size of the Bi cores form larger plasmon resonators, lowering the plasmon frequency and energy. Plasmons are also typically sensitive to the dielectric properties of the surrounding material. Fig. 5b-c show that increasing the thickness of the BiOCl shell causes a small redshift in the peak energies, as well as an increase in their intensities (Fig. 5b-c). This enhanced scattering cross section for thicker shells is an interesting phenomenon in itself, and is likely to be the result of the extended high refractive index around the plasmonic core. To determine the plasmonic enhancement qualitatively, the optical responses under unpolarized light excitation of two particles of different sizes were simulated: a 46 nm core + 6 nm shell and a 93 nm core + 9 nm shell radii, the same as the experimentally-measured particles in Fig. 4a-h, immersed in water. Fig. 5d shows the resulting electromagnetic far-field scattering spectra, from which we can distinguish a single LSPR at 2.6 eV for the small particle and two resonances at 1.8 eV and 2.7 eV for the large one.

A closer look at the electromagnetic response of these core-shell systems can be obtained by investigating the behavior of the electromagnetic near-field in their surroundings. We have calculated the near-field enhancement spectra at three locations around the particles labelled X, O, and Z as displayed in the inset of Fig. 5d. The corresponding induced near-field spectra shown in Fig. 5e-f are noticeably different from the far-field ones; this can be explained by the dark plasmon modes sustained by the particles which do not radiate and thus have no far-field signature. We observe substantial variations from the analysis of three locations around the particles: X, located far from the TiO_2 substrate, Z in the tiny gap between the BiOCl shell and the TiO_2 substrate, and O halfway between the two previous points. Remarkably, in both cases, greater enhancement factors are obtained at the Z position; a factor of 9.1 for the small particle at 2.6 eV (higher than 7 within the range between 2 eV and 3 eV) and a factor of 6.8 at 1.5 eV for the large one (above 5.5 in the range 1.0–2.3 eV). Fig. 5g-h shows the quantitative mapping of the calculated enhancement factor around the particles at 2.6 eV (small) and 1.5 eV (large), revealing in both cases the localization of the highest enhancement in the vicinity of the particle-substrate/template interface. This observation eventually explains the synergistic effect of the core Bi-shell BiOCl-TiO_2 substrate in the CO_2 reduction reaction (CO_2RR). The above results are further corroborated by the wavelength-dependent local field enhancement mapping as shown in Fig. S16. As observed, the smaller particles show higher local E-field < 2.48 eV (> 500 nm) at Z-position, while the local E-field enhancement for larger particles is in the range of < 2.95 eV (> 420 nm) (The green curves in Fig. S16a-b).

Based on measurements with different light wavelengths by using band-pass filters (Note S2), the AQE is zero under 600 nm light illumination and 0.28 % under 500 nm, respectively. 400 nm light illumination brings the AQE up to 1.14 %, which then slightly increases to 1.36 % at 380 nm. The observed contribution of the surface defects from TiO_2 (low density, Note S6) with PL peak at ~ 600 nm (Fig. 1d) and/or Bi plasmon-generated hot electrons sitting at 528 nm, 752 nm, or 827 nm (Figs. 4d, 4k), which are photoexcitable by 500 nm light, on the photocatalytic performance is quite low (AQE 0.28 %). However, when the photoexcitation wavelength reduces to $\leq$ 400 nm, the AQE undergoes a notable increase to $\geq$1.14 %. This is primarily linked to the generation of active charges (electrons/holes) from the absorption of light on the electronic band gaps of TiO_2 (2.78 eV/446 nm) and BiOCl (near UV range from high density defect states, Note S6). These electrons/holes

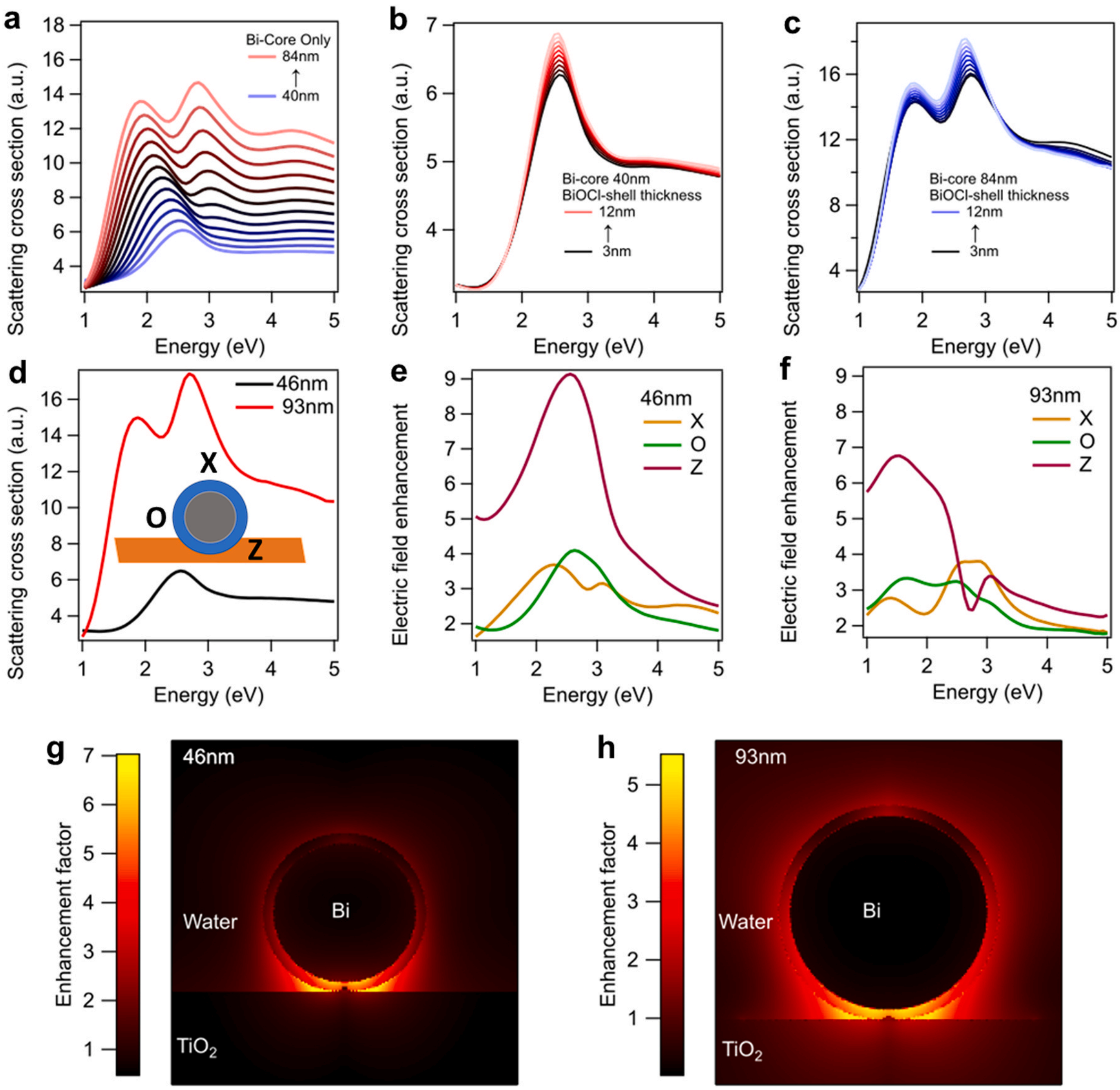

Fig. 5. Size-dependent electromagnetic response. (a) Far-field scattering spectra for uncoated Bi nanospheres with radii ranging from 40 nm to 84 nm. (b) 40 nm core Bi coated with BiOCl shells of thicknesses from 3 nm to 12 nm and (c) same as b for an 84-nm Bi core. (d) Far-field scattering spectra of core-shell Bi-BiOCl on TiO_2 nano-substrate with radii of 46 nm (black) and 93 nm (red), the inset is a scheme of the heterojunction: Bi core in grey, BiOCl shell in blue and TiO_2 substrate in orange. (e) and (f) the near-field enhancement factor spectra measured at the X, O and Z locations as depicted in the inset of (d) for 46-nm and 93-nm particles, respectively. (g) Calculated maps of the near-field enhancement factors around 46-nm (left) and (h) 93-nm (right) core-shell particles on TiO_2 substrate, immersed in water.

will be well separated at the TiO_2-BiOCl heterojunction and hence contribute to the redox reaction there, which will be explored and discussed in more details below. Note that the existence of the Bi plasmon obviously broadens the light absorption of TiO_2 from an edge of ~420 nm shifting to ~600 nm (Fig. 1c). The wavelength-dependent AQE implies that the TiO_2-BiOCl junction, which mainly harvests shorter-wavelength light, contributes to the efficiency of CO_2RR. On the other hand, the Bi plasmon can be excited by UV–visible-near IR light to generate both hot electrons and strong local E-field at the Z location (Fig. 5). However, the above AQE results indicate that hot electrons play a minor role in CO_2RR; then, the role of a strong E-field in CO_2RR will be investigated using DFT calculations. Specifically, we will focus on the experimental observation of the conversion of CO_2 into the sole carbon product of CH_3OH, and examine how the presence of a strong E-field affects this process. Therefore, the conversion of CO_2 into CH_3OH mainly occurs at the Z location, which is the BiOCl-TiO_2 interface where a higher local E-field and photo-excited electrons from TiO_2 NSs coexist, as substantiated by DFT calculations in the following section.

2.4. *Proposed reaction mechanism with DFT analysis*

The key idea in our plasmonic CO_2 transformation over a TiO_2-BiOCl-Bi heterojunction is to drive the kinetically challenging multielectrons/protons-assisted production of methanol. Under light excitation, the enhanced E-field at the Z location interface and the established TiO_2-BiOCl junction can promote the electron-hole separation and reduce their recombination, resulting in a longer lifetime of photoinduced charge carriers. TRPL of the TiO_2-BiOCl-Bi heterojunction was studied to unravel the nature of photoinduced excitons, their photodynamics and potential contribution to the improved photoactivity for CO_2 reduction. Mathematical fitting of TRPL data in Fig. 6a estimates the average carrier lifetime (7.93 ns) for the TiO_2-BiOCl-Bi fresh sample, which is much shorter than that of TiO_2 (8.82 ns) at 420 nm excitation, whereas BiOCl has a lifetime of ~8.92 ns at an excitation wavelength of 361 nm. The reduced PL carrier lifetime of the TiO_2-BiOCl-Bi sample could be associated with effective spatial charge separation and transfer across the heterojunction interface [43,44], leading to improved

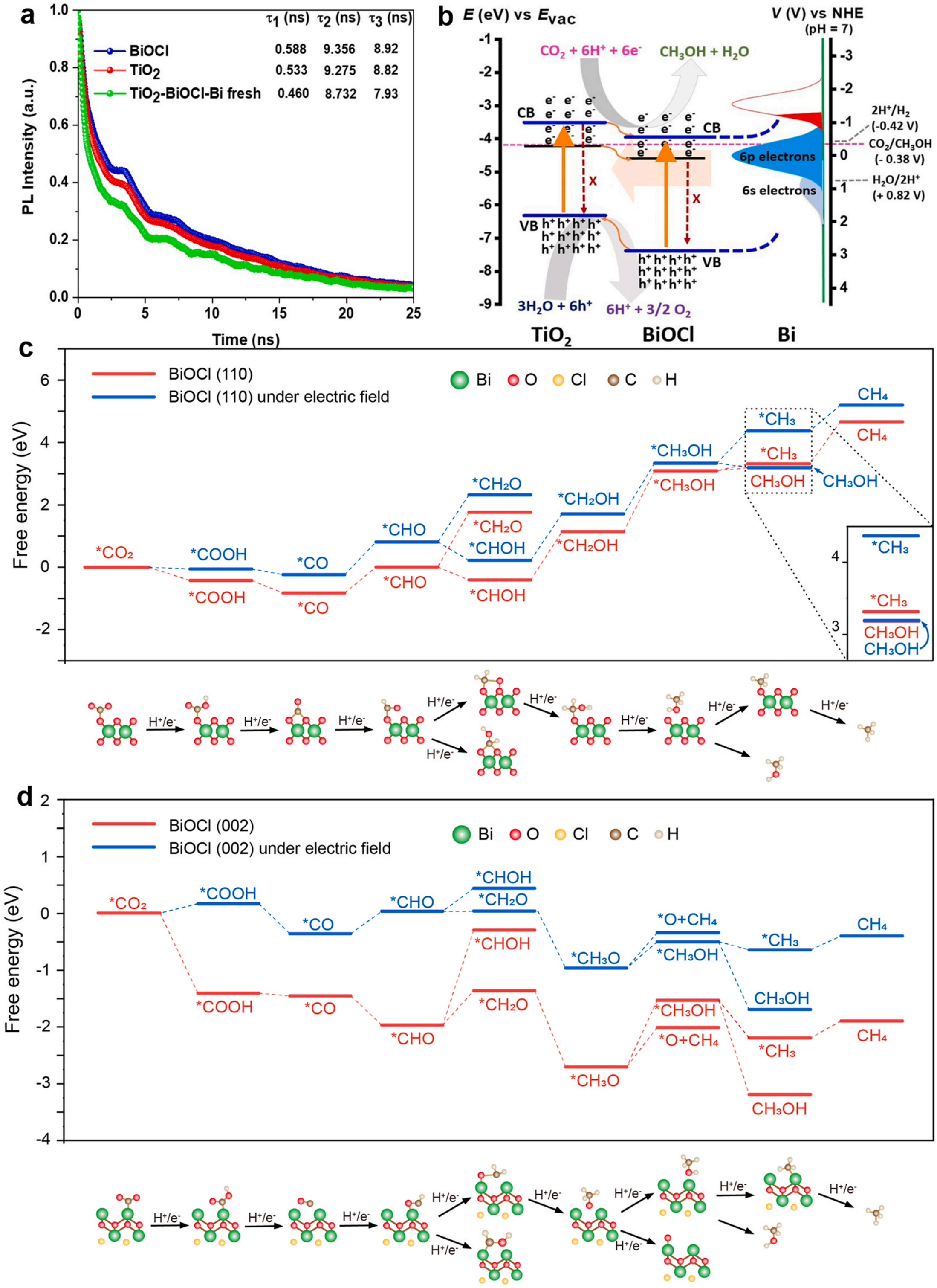

Fig. 6. (a) TRPL profiles for bare BiOCl, bare TiO_2 and TiO_2-BiOCl-Bi fresh photocatalysts within this work for photodynamics of TiO_2-BiOCl-Bi heterostructure. Excitation wavelength for both bare TiO_2 and TiO_2-BiOCl-Bi fresh was 420 nm while it was 361 nm for bare BiOCl sample. Summarized fitted parameters are shown inside Fig. 6a. The average carrier lifetime (τ_3) of the studied photocatalysts was determined by fitting a bi-functional exponential decay formula. The calculation procedure is outlined in **Note S9**. (b) Schematic energy diagram of a simplified band structure for the TiO_2/BiOCl heterojunction. Defects energy levels for TiO_2 and BiOCl (black solid line) were estimated to be nearly −0.35 and 0.16 V in the scale of NHE, respectively. To make the energy scale more easily readable and comparable, both E_{vac} and NHE scale settings are plotted where the potential energy next to CO_2 transformed products is in V versus NHE at pH = 7. The pink-colored striped line represents the CO_2 redox potential on NHE scale. The deep-red striped lines marked X correspond to charge recombination path unlikely to happen. The light-orange arrow mark indicates the localization of E-field at TiO_2-BiOCl interface whereas the upward band bending of BiOCl towards Bi indicates that the electrons in the CB move away from the BiOCl-Bi interface. Free energy diagram for CO_2RR on BiOCl (c) (110) and (d) (002) facets calculated by DFT, where the E-field perturbation (867.93 V/m under ×8.5 enhancement) was applied for the blue lines and was absent for the red lines.

photoactivity. However, the longer PL lifetimes of the BiOCl and TiO_2 samples imply that the photoinduced charge carriers cannot transfer rapidly and thus result in charge recombination. This conclusion is in line with the improved photocatalytic activity.

Methanol generation from CO_2 reduction follows a multi-electron/proton concerted path, which is complicated but thermodynamically favorable [45,46]. Fig. 6b shows the energy band diagrams with bandgaps of 2.78 and 3.43 eV for TiO_2 and BiOCl, respectively (Fig. S17, Note S7). The conduction band (CB) potential for TiO_2 and BiOCl is −0.97 and −0.54 V (vs normal hydrogen electrode (NHE)), while the valence band (VB) position is at 1.81 and 2.88 V (vs NHE), respectively. Calculation of band potentials can be found elsewhere (Note S5–6, Fig. S18). Upon light illumination, electrons pump into the CB, leaving holes in the VB. The CB position of BiOCl is more negative than that of TiO_2, allowing the migration of electrons from the CB of TiO_2 to the CB of BiOCl, whereas the photo-generated holes in the VB of BiOCl can easily transfer to the VB of TiO_2. Under the synergistic effects of the LSPR and BiOCl/TiO_2 heterojunction thanks to the photon energy and local density-of-states in the metal [47], a desirable effective charge carrier separation and reaction path tuning can be achieved, which allows more energetic electrons and holes participation in the E-field tuned reaction. This is indicative that the core Bi-shell BiOCl NPs on TiO_2 NSs contain electrons with higher energy than that of the reduction potential of CO_2 [45]. Note that the electrons from defect energy levels, after being photoexcited from the VB or migrated from the CB of TiO_2, can easily migrate to lower energy states (defect sites) of BiOCl, which is much more positive than the CO_2 reduction potential. Under resonant illumination, electrons in these defect states can be pumped upwards into the CB of BiOCl, after which these electrons are ready to contribute to the CO_2 reduction. The efficiency of this process depends on the illumination light wavelength, where the shorter wavelengths (e.g. 400 nm) contribute more efficiently than the longer ones, as can be seen from the AQE results (Note S2). Conversely, the Bi LSPR are excited by light of relatively long wavelengths, and they deliver the 7–9 times enhanced E-fields as demonstrated above and in Fig. S16. The plasmon-enhanced E-fields generated by long-wavelength illumination complement the short-wavelength generation of energetic charge carriers in the TiO_2. Therefore, the different components in the TiO_2-BiOCl-Bi system absorb and utilize a broad range of the visible spectrum for their complementary functions.

Photoinduced electrons from the CB of BiOCl do not combine with the holes on the VB of TiO_2 due to the type-II heterojunction formed, and is expected to play a key role in the reduction of CO_2 molecules under plasmon perturbation. Non-selective CH_3OH paths occur when the methanol concentration reaches an appreciable value in the solution and it begins competing with water for VB holes in TiO_2 NSs [48]. Under this condition, it is thinkable that methanol oxidation by the holes in the VB of TiO_2 NSs, and water reduction by electrons from the CB of BiOCl NPs could convert methanol into other C-based products and facilitate the hydrogen evolution reaction. However, our near-zero observation of other C-based products and low amounts of H_2 by-product (Fig. 3) thus confirms that the CO_2-to-methanol conversion here takes place without backward reaction, e.g. without methanol oxidation.

To elucidate the underlying reaction mechanism, DFT calculations were performed on the CO_2RR performance of the TiO_2-BiOCl-Bi catalyst. Since both the photogenerated electrons of TiO_2 and the hot electrons from Bi NPs migrate to the CB of the BiOCl layer, the CO_2RR occurs on the BiOCl layer. Here, given the exposed BiOCl (110) and (002) facets identified by STEM (Fig. 2**c**), the above exposed facets were considered for the CO_2RR free energy calculation in this study (Note S8). Fig. 6c-d depicts the free energy diagrams of the two facets. The free energy diagram of the intermediates varies with the exposed surface, due to the highly anisotropic tetragonal layered structure of BiOCl [49]. In Fig. 6c-d, the (110) facet tends to allow *CHO hydrogenation to form *CHOH, attributable to surface Bi on the (110) facet adsorbing C from *CHO, while the (002) facet is more likely to form *CH_2O from *CHO which is ascribed to O adsorption from *CHO on the surface of the (002) facet. In addition, the Gibbs free energy (△G) of the respective reactions is 1.95 eV (*CH_2OH→*CH_3OH) on the (110) facet and 0.81 eV (*CH_3O→*CH_4) on the (002) facet, which are the rate-determining steps for CO_2RR on these facets. The conclusion for the (110) facet is consistent with a previous study in which the protonation step to form *CH_3OH for BiOCl was considered to be the rate-determining step in the overall CO_2RR process [50]. Moreover, Bi acts as a plasmonic metallic core, providing a photogenerated E-field for the BiOCl shell, and the blue lines in Fig. 6c-d show the free energies under a photogenerated E-field perturbation. Although the E-field does not have a significant impact on each reaction path, it can reduce the energy barrier of a specific reaction step between the polyatomic intermediates. Benefiting from this, the energy barrier of the next reaction of *CH_3OH on the (110) facet shows a difference under the E-field perturbation, which makes it more difficult for the further reduction of *CH_3OH to CH_4, thus improving *CH_3OH desorption to form methanol in high selectivity. In addition, the energy barrier for the rate-determining step on the (002) facet is reduced under the E-field perturbation. However, the energy barrier reduction of *CH_3O→*CH_3OH (△G reduced from 1.17 eV to 0.46 eV) with higher molecular mass compared with *CH_3O→CH_4 (△G reduced from 0.81 eV to 0.57 eV) is more significant, and prevents the reduction of *CH_3O to CH_4 and results in dramatically increased selectivity towards CH_3OH production.

3. Conclusions

In summary, TiO_2 NSs decorated with plasmonic Bi-BiOCl NPs were designed and used for selective photocatalytic reduction of CO_2 to CH_3OH. This study describes how photoejected electrons can induce the CO_2 reduction reaction selectively on the TiO_2-BiOCl heterojunction. Noble-metal free plasmonic Bi NPs lead to significantly enhanced light absorption due to LSPR effects, and modulate the TiO_2-BiOCl heterojunction which collectively contributes to the efficient electron-hole separation and localization at the heterointerfaces. The enhanced electromagnetic fields from the Bi plasmons can positively impact the catalytic activity of the BiOCl shells. Under AM 1.5 G solar illumination, the optimal plasmonic heterojunction leads to a high CH_3OH generation rate up to 235.78 μmol g^{-1} h^{-1} with a high selectivity of ~90 % of sole methanol as the carbon product. Furthermore, long-lasting performance was demonstrated. Quantitative simulations and theoretical calculations reveal that the local Bi-plasmon induced E-field plays a key role in tailoring the CO_2 reduction paths towards methanol at the TiO_2-BiOCl heterojunction. The above results in this work provide an exciting route for selective reduction of CO_2 into CH_3OH by surface plasmon resonance-enhanced photocatalysis.

4. Methods

4.1. Materials

Titanium(IV) isopropoxide (≥97 %, Sigma Aldrich), diethylenetriamine (≥99 %, Sigma Aldrich), propan-2-ol (≥99.5 %, Chem-Supply), $BiCl_3$ (≥98 %, Sigma Aldrich), polyvinylpyrrolidone (PVP, M_w ~55,000, Sigma Aldrich), N,N-dimethylformamide (≥99.8 %, Sigma Aldrich), $NaBH_4$ (≥98 %, Sigma Aldrich), $Bi(NO_3)_3$•5 H_2O (≥98.0 %, Sigma Aldrich), glycerol (≥99.0 %, Sigma Aldrich), ethyl alcohol (HPLC/spectrophotometric grade, Sigma Aldrich) and $NaHCO_3$ (≥99.7 %, Chem-Supply), were used without further purification. Carbon dioxide gas (99.99 %, high purity grade, compressed) was purchased from BOC Gas (Australia). Deionized water (18.2 MΩ·cm) was used throughout the experiments.

5. Characterization

Powder X-ray diffraction (pXRD) patterns were collected by using a

PANalytical Empyrean diffractometer with Cu-Kα radiation ($\lambda = 1.54056$ Å) operated at 40 kV, 40 mA and a scanning speed of 0.022255°/s. Scanning electron microscopy (SEM) was performed on a Zeiss UltraPlus FESEM at 3 kV. The photocatalysts were transferred to an appended ultrahigh vacuum chamber equipped with a VG/Scienta R3000 electron energy analyzer and a monochromatic Al-Kα X-ray source for high-resolution X-ray photoelectron spectroscopy (XPS) studies. Transmission electron microscopy (TEM) was performed using a Hitachi HF5000 Cs-STEM/TEM at 200 kV. Ultraviolet–visible (UV-Vis) diffuse reflectance spectroscopy (DRS) was carried out on a PDA UV/Vis Lambda 465 Spectrophotometer (PerkinElmer). High angle annular dark-field (HAADF) scanning transmission electron microscopy (STEM) imaging and core-loss electron energy-loss spectroscopy (EELS) were carried out using a ThermoFisher Themis-Z double-corrected microscope operated at 300 kV equipped with ChemiSTEM (Super-X) X-ray detectors and a Gatan Quantum ER/965 GIF. Monochromated EELS for plasmon characterisation was performed on a ThermoFisher Titan S/TEM with Tridiem EELS detector, operated at 80 kV, with a ~1 nm electron beam and an energy resolution of 65 meV. A pre-measured, high-quality vacuum spectrum was fitted and subtracted as background signal. Acquisition using binned gain averaging was performed [51]. Plasmons simulations were performed using the Boundary Element Method [52] as successfully demonstrated before [53] and described in more detail in the Supplement. The photoluminescence (PL) spectra were measured using a Horiba T64000 spectrometer system equipped with a Kimmon 325 nm HeCd laser source. Time-Resolved Photoluminescence (TRPL) curves were captured at room temperature using a Horiba iHR 320 mm spectrophotometer equipped with a compact single-photon silicon detector (PPD-900, detection range between 350 and 920 nm). A 485-nm picosecond pulse laser (Horiba DeltaDiode) was used as excitation source with a pulse width of 80 ps. The laser light was focused on the TiO_2, BiOCl, fresh, and recycled samples through an Olympus BX53 microscope equipped with a 50x objective lens and an X-Y micropositioner. All measurements were done with a 16.6 MHz repetition rate. The lifetimes were calculated by fitting the decay curves with a bi-exponential decay function. Mott-Schottky analysis was carried out using a PARSTAT 3000 electrochemical workstation (Princeton Applied Research). Gas chromatography-thermal conductivity detection (GC-TCD) was performed on a Nexis GC-2030 gas chromatograph (Shimazu) equipped with a thermal conductivity detector using Shin-Carbon ST Micropacked GC Column cat.# 19808 (Restek). Gas chromatography-flame ionization detection (GC-FID) was performed on a headspace GC 7890 A gas chromatograph (Agilent) equipped with a flame ionization detector using J&W DB-WAX GC Column (Agilent). The end products after photocatalytic reaction were also determined by a 7010 Triple Quadruple GC/MS/MS (Agilent) instrument using same column.

6. Synthesis

TiO_2 ultrathin NSs were prepared by a solvothermal method as reported before [18]. A 0.036 mL diethylenetriamine was added to 33.6 mL of propan-2-ol. After the solution was gently stirred for 10 min, 1.2 mL of titanium (IV) isopropoxide was added. The reaction solution was then transferred to a 48 mL Teflon-lined stainless steel autoclave and kept in an electric oven at 200 °C for 24 h. After cooling naturally to room temperature, white precipitate was collected by centrifugation, washed thoroughly with ethanol, and dried at 60 °C overnight. The products were calcined in air at 400 °C for 8 h at a ramping rate of 10 °C min^{-1}. Bare BiOCl was prepared from an existing method with slight modification as: a mixture of 30 mL methanol and 1 mL HCl solution at pH = 1 was prepared [54]. After 30-min stirring, the colorless solution was heated in a high-pressure reactor at 150 °C for 3 h, followed by centrifugation and washing with deionized water and ethanol for several times. The TiO_2-BiOCl-Bi heterojunction was prepared by a borohydride reduction method as reported [55], followed by Ar gas treatment. TB 20-post-Ar (TiO_2:Bi=20:1, molar ratio), TB 15-post-Ar (TiO_2:Bi=15:1, molar ratio), or TB 10-post-Ar (TiO_2:Bi=10:1, molar ratio) was synthesized as below: 11.81 mg (0.0375 mmol), 15.75 mg (0.05 mmol), or 23.62 mg (0.075 mmol) $BiCl_3$, respectively, was dissolved with 27.75 mg PVP in 10 mL of N, N-Dimethylformamide (DMF), and then 60.00 mg (0.75 mmol) of the obtained TiO_2 was added to the suspension. The obtained suspension was degassed using nitrogen for 30 min and stirred for 2 h. In addition, corresponding to the synthesis of TB 20-post-Ar (TiO_2:Bi=20:1, molar ratio), TB 15-post-Ar (TiO_2:Bi=15:1, molar ratio), or TB 10-post-Ar (TiO_2:Bi=10:1, molar ratio), 0.20 mL, 0.15 mL or 0.10 mL of 1.0 M $NaBH_4$ aqueous solution was injected into 10 mL DMF and also degassed using nitrogen for 30 min. Then, the DMF solution containing $NaBH_4$ was added into the mixture suspension with constant stirring under flowing nitrogen and then continued stirring for another 20 min after addition. The products were precipitated by adding acetone, collected by centrifugation (Eppendorf 5430) and then dried in a vacuum oven (TVO-35, Thermoline L+M) for 4 h at room temperature. The products were calcined in Argon at 400 °C for 2 h at a ramping rate of 10 °C min^{-1}. Pure BiOCl-Bi was obtained using the same procedure except for not adding TiO_2. The effect of Ar annealing on the heterojunction was studied at a constant temperature with variable exposure lengths of time.

7. Photocatalytic experiments

Designed amounts of the as-prepared photocatalyst were added into 5 mL 0.2 M $NaHCO_3$ in a quartz bottle tightly sealed by a septum and parafilm. The suspension was sonicated (B2500R-DTH, Branson) for 10 min and then degassed using CO_2 for 30 min under stirring in the dark. After that, the suspension was illuminated by 300 W Xenon lamp (PLS-SXE300D, Perfect Light) with AM 1.5 G filter for 4, 8, 12, 16, 20, and 24 h under stirring, respectively. The gas and liquid products were analyzed by GC-TCD, GC-FID, and GC-MS-MS, respectively whereas experimental procedures can be found elsewhere [56]. All experiments were performed in triplicate. The photocatalysts were collected after photocatalytic reaction and regenerated through $NaBH_4$ reduction. Afterwards, the regenerated photocatalysts were tested for the subsequent cycle of CO_2 photoreduction. The recyclability of TiO_2-BiOCl-Bi photocatalysts was examined in three consecutive cycles as described above.

CRediT authorship contribution statement

Haijiao Lu and **Nasir Uddin** contributed to materials preparation, performing photocatalytic experiments, analysing data, and writing manuscript. **Zhehao Sun** carried out DFT experiment, analyzed data, and wrote the manuscript. **Zibin Chen**, **Xiaozhou Liao** and **Simon P. Ringer** performed STEM and core-loss EELS experiments and wrote the manuscript. **Zackaria Mahfoud** carried out BEM simulations. **Yilan Wu** and **Xiu Song Zhao** performed HRTEM experiments. **Ary Anggara Wibowo** and **Hieu T. Nguyen** performed TRPL measurement. **Zhicheng Su** and **Hark Hoe Tan** performed PL measurements. **Xinmao Yin**, **Chi Sin Tang**, and **Andrew T.S. Wee** assisted in performing XPS measurements. **Michel Bosman** carried out monochromated EELS measurement, analyzed data and wrote the manuscript. **Zongyou Yin** conceived and supervised the project, analyzed data, and wrote the manuscript.

Declaration of Competing Interest

The authors declare no conflict of interest.

Data Availability

Data will be made available on request.

Acknowledgements

We gratefully acknowledge financial support from the Australian Research Council (DP190100295) and the ANU Futures Scheme (Q4601024). ZM and MB kindly acknowledge support from Hue Thi Bich Do (National University of Singapore) for the plasmon simulations, as well as support from the Ministry of Education (MOE) Singapore, via the Academic Research Fund AcRF Tier 2 (project numbers MOE2019-T2-1-179 and MOE-T2EP50122-0016). The authors acknowledge the Singapore Synchrotron Light Source (SSLS) for providing the facilities necessary for conducting the experiments. The SSLS is a National Research Infrastructure under the National Research Foundation, Singapore. This research was undertaken with the assistance of resources provided by the National Computational In-frastructure (NCI) facilities at the Australian National University, which were allocated through the National Computational Merit Allocation Scheme (NCMAS), ANU Merit Allocation Scheme (ANUMAS) and NCI's Adapter Allocation Scheme.

Appendix A. Supporting information

Supplementary data associated with this article can be found in the online version at doi:10.1016/j.nanoen.2023.108684.

References

[1] V. Grewe, A. Gangoli Rao, T. Grönstedt, C. Xisto, F. Linke, J. Melkert, J. Middel, B. Ohlenforst, S. Blakey, S. Christie, Nat. Commun. 12 (2021) 1.
[2] J. Chen, Y. Fei, Z. Wan, J. Environ. Manag. 242 (2019) 31.
[3] A.W. Schäfer, S.R. Barrett, K. Doyme, L.M. Dray, A.R. Gnadt, R. Self, A. O`Sullivan, A.P. Synodinos, A.J. Torija, Nat. Energy 4 (2019) 160.
[4] A. Kumar, P. Daw, D. Milstein, Chem. Rev. 122 (2021) 385.
[5] Z. Zhang, C. Mao, D.M. Meira, P.N. Duchesne, A.A. Tountas, Z. Li, C. Qiu, S.L. Tang, R. Song, X. Ding, J. Sun, J. Yu, J.Y. Howe, W. Tu, L. Wang, G.A. Ozin, Nat. Commun. 13 (2022) 1512.
[6] M. Gondal, A. Lais, M. Dastageer, D. Yang, K. Shen, X. Chang, Int. J. Energy Res. 41 (2017) 2162.
[7] R.C. Sahoo, H. Lu, D. Garg, Z. Yin, H.R. Matte, Carbon 192 (2022) 101.
[8] H. Lu, J. Tournet, K. Dastafkan, Y. Liu, Y.H. Ng, S.K. Karuturi, C. Zhao, Z. Yin, Chem. Rev. 121 (2021) 10271.
[9] S. Linic, P. Christopher, D.B. Ingram, Nat. Mater. 10 (2011) 911.
[10] M.L. Brongersma, N.J. Halas, P. Nordlander, Nat. Nanotechnol. 10 (2015) 25.
[11] U. Aslam, V.G. Rao, S. Chavez, S. Linic, Nat. Catal. 1 (2018) 656.
[12] H. Wang, H. Rong, D. Wang, X. Li, E. Zhang, X. Wan, B. Bai, M. Xu, J. Liu, J. Liu, Small 16 (2020) 2000426.
[13] N.Q. Thang, A. Sabbah, L.-C. Chen, K.-H. Chen, C.M. Thi, P. Van Viet, Chem. Eng. Sci. 229 (2021), 116049.
[14] Q. Wang, K. Chen, S. Wang, Y. Li, L. Zeng, C. Ma, D. Jiang, L. Zhu, X. Xu, J. Alloy. Compds. 887 (2021), 161457.
[15] A. Ziarati, A. Badiei, R. Luque, M. Dadras, T. Burgi, ACS Sustain. Chem. Eng. 8 (2020) 3689.
[16] Z. Wei, F. Yue, Z. Jin, Z. Fengxia, S. Zhenhuan, D. Benlin, D.Y. Leung, Z. Lili, X. Jiming, ACS Appl. Energy Mater. 2 (2018) 694.
[17] C. Bhattacharya, S.E. Saji, A. Mohan, V. Madav, G. Jia, Z. Yin, Adv. Energy Mater. 10 (2020) 2002402.
[18] J.S. Chen, Y.L. Tan, C.M. Li, Y.L. Cheah, D. Luan, S. Madhavi, F.Y.C. Boey, L. A. Archer, X.W. Lou, J. Am. Chem. Soc. 132 (2010) 6124.
[19] M. Li, Y. Chen, W. Li, X. Li, H. Tian, X. Wei, Z. Ren, G. Han, Small 13 (2017) 1604115.
[20] J. Hu, W. Fan, W. Ye, C. Huang, X. Qiu, Appl. Catal. B: Environ. 158 (2014) 182.
[21] Z. Yang, D. Wang, Y. Zhang, Z. Feng, L. Liu, W. Wang, ACS Appl. Mater. Interfaces 12 (2020) 8604.
[22] L.J. Ma, H.Q. Wu, B.Y. Chen, G. Wang, B.X. Lei, D. Zhang, D.B. Kuang, Adv. Mater. Interfaces (2022) 2102522.
[23] L. Li, Y.W. Yang, G.H. Li, L.D. Zhang, Small 2 (2006) 548.
[24] N. Hussain, T. Liang, Q. Zhang, T. Anwar, Y. Huang, J. Lang, K. Huang, H. Wu, Small 13 (2017) 1701349.
[25] X. Cheng, Y. Sun, D. Li, H. Yang, F. Chen, F. Huang, Y. Jiang, Y. Wu, X. An, Y. Yu, Adv. Energy Mater. 11 (2021) 2102263.
[26] Y. Wang, J. Jin, W. Chu, D. Cahen, T. He, ACS Appl. Mater. Interfaces 10 (2018) 15304.
[27] L. Chen, E. Alarcón-Lladó, M. Hettick, I.D. Sharp, Y. Lin, A. Javey, J.W. Ager, J. Phys. Chem. C 117 (2013) 21635.
[28] M. Oku, H. Matsuta, K. Wagatsuma, Y. Waseda, S. Kohiki, J. Electron Spectrosc. Relat. Phenom. 105 (1999) 211.
[29] D. Hou, X. Hu, P. Hu, W. Zhang, M. Zhang, Y. Huang, Nanoscale 5 (2013) 9764.
[30] Z. Zhang, M. Chi, G.M. Veith, P. Zhang, D.A. Lutterman, J. Rosenthal, S. H. Overbury, S. Dai, H. Zhu, ACS Catal. 6 (2016) 6255.
[31] G. Jiang, X. Li, M. Lan, T. Shen, X. Lv, F. Dong, S. Zhang, Appl. Catal. B: Environ. 205 (2017) 532.
[32] W. Gao, J. Lu, S. Zhang, X. Zhang, Z. Wang, W. Qin, J. Wang, W. Zhou, H. Liu, Y. Sang, Adv. Sci. 6 (2019) 1901244.
[33] D.K. Pallotti, L. Passoni, P. Maddalena, F. Di Fonzo, S. Lettieri, J. Phys. Chem. C 121 (2017) 9011.
[34] M.V. Dozzi, C. D`Andrea, B. Ohtani, G. Valentini, E. Selli, J. Phys. Chem. C 117 (2013) 25586.
[35] Y. Liu, M. Wang, D. Li, F. Fang, W. Huang, Appl. Surf. Sci. 540 (2021), 148330.
[36] Y. Yan, H. Yang, Z. Yi, T. Xian, Catalysts 9 (2019) 795.
[37] E.B. Creel, E.R. Corson, J. Eichhorn, R. Kostecki, J.J. Urban, B.D. McCloskey, ACS Energy Lett. 4 (2019) 1098.
[38] Z. Jiao, M. Shang, J. Liu, G. Lu, X. Wang, Y. Bi, Nano Energy 31 (2017) 96.
[39] F. Dong, Q. Li, Y. Sun, W.-K. Ho, ACS Catal. 4 (2014) 4341.
[40] M. Bosman, V.J. Keast, M. Watanabe, A.I. Maaroof, M.B. Cortie, Nanotechnology 18 (2007), 165505.
[41] M. Sayed, J. Yu, G. Liu, M. Jaroniec, Chem. Rev. 122 (2022) 10484–10537.
[42] K. Awazu, M. Fujimaki, C. Rockstuhl, J. Tominaga, H. Murakami, Y. Ohki, N. Yoshida, T. Watanabe, J. Am. Chem. Soc. 130 (2008) 1676.
[43] M. Ochoa, S.C. Yang, S. Nishiwaki, A.N. Tiwari, R. Carron, Adv. Energy Mater. 12 (2022) 2102800.
[44] Y. Zhang, J. Zhao, H. Wang, B. Xiao, W. Zhang, X. Zhao, T. Lv, M. Thangamuthu, J. Zhang, Y. Guo, Nat. Commun. 13 (2022) 1.
[45] N. Uddin, H. Zhang, Y. Du, G. Jia, S. Wang, Z. Yin, Adv. Mater. 32 (2020) 1905739.
[46] W. Zhang, A.R. Mohamed, W.J. Ong, Angew. Chem. Int. Ed. 59 (2020) 22894.
[47] Y. Zhang, Z. Xu, Q. Wang, W. Hao, X. Zhai, X. Fei, X. Huang, Y. Bi, Appl. Catal. B: Environ. 299 (2021), 120679.
[48] A. Yahaya, M. Gondal, A. Hameed, Chem. Phys. Lett. 400 (2004) 206.
[49] S. Bai, X. Li, Q. Kong, R. Long, C. Wang, J. Jiang, Y. Xiong, Adv. Mater. 27 (2015) 3444.
[50] G. Gao, Y. Jiao, E.R. Waclawik, A. Du, J. Am. Chem. Soc. 138 (2016) 6292.
[51] M. Bosman, V.J. Keast, Ultramicroscopy 108 (2008) 837.
[52] U. Hohenester, A. Trügler, Comput. Phys. Commun. 183 (2012) 370.
[53] M. Asbahi, Z. Mahfoud, S.B. Dolmanan, W. Wu, Z. Dong, F. Wang, M.S. Saifullah, S. Tripathy, K.S. Chong, M. Bosman, ACS Appl. Mater. Interfaces 11 (2019) 45207.
[54] D. Sun, J. Li, L. He, B. Zhao, T. Wang, R. Li, S. Yin, Z. Feng, T. Sato, CrystEngComm 16 (2014) 7564.
[55] Y. Wang, B.H. Hong, K.S. Kim, J. Phys. Chem. B 109 (2005) 7067.
[56] N. Uddin, J. Langley, C. Zhang, A.K. Fung, H. Lu, X. Yin, J. Liu, Z. Wan, H. T. Nguyen, Y. Li, Appl. Catal. B: Environ. 292 (2021), 120212.

Dr. Haijiao Lu obtained her dual bachelor's degrees in Science from Nankai University and in Engineering from Tianjin University in 2014, and PhD from Tianjin University in 2019. She was a visiting PhD student at the University of Cambridge in 2017–2019. She worked as a postdoctoral research fellow at the Australian National University in 2019–2021, and then the University of Queensland from July 2021. Since Jan 2023, she has been working as an ARC DECRA Fellow at the University of Queensland. Her work is characterized by interdisciplinary research, which lies at the intersection of materials science, photo(electro)catalysis, and chemical engineering.

Dr. Nasir Uddin received his BS in Chemical Engineering from Shah Jalal University of Science and Technology, MS in Chemical Engineering from the University of New Mexico, and PhD from the Australian National University. He worked on the development of functional photocatalytic 2D nanomaterials for hydrogen energy production from light alcohol splitting. He has gained expertise in photocatalytic plasmonic and heterogeneous catalytic systems, starting from materials preparation to characterization using various cutting-edge instruments. After his PhD studies, he joined the Australian National University Battery Storage and Grid Integration Program as a Postdoctoral Fellow.

Dr. Zibin Chen earned his Ph.D. degree from the University of Sydney in 2017. Presently, he holds the position of Assistant Professor within the Department of Industrial and Systems Engineering at the Hong Kong Polytechnic University. His area of specialization revolves around electron microscopy, with a specific focus on investigating the structure-property relationship in newly developed functional ferroelectric materials and additively manufactured metallic materials.

Dr. Michel Bosman is Associate Professor at the Materials Science and Engineering department at the National University of Singapore, specializing in scanning transmission electron microscopy (STEM). He was trained at Delft University of Technology (the Netherlands) and at the University of Sydney, with postdoctoral experience in Australia, the UK and Singapore. His research focuses on high-resolution imaging of materials and on experimental nano-optical techniques in the STEM.

Associate Professor Zongyou Yin obtained his B.S. and M.S. degrees at Jilin University in China, and his Ph.D. at Nanyang Technological University (NTU) in Singapore, followed by postdoctoral experience at NTU and IMRE (Singapore), MIT and then Harvard University. Dr Yin started his own Research Group at Australian National Univesrity (ANU) in 2017. His group's research is interdisciplinary, encompassing AI-driven materials innovations, nano-to-atomic materials science, fundamental relationship among materials-structures-devices, and synergistic integration of multi-functions for energy and wearable applications.